Laplace-domain Fluid Structure Interaction solutions for water hammer waves in a pipe

Alexandre Bayle, Franck Plouraboué

Laplace-domain Fluid Structure Interaction solutions for water hammer waves in a pipe

ALEXANDRE BAYLE[1] and FRANCK PLOURABOUE corresponding author
Email:fplourab@imft.fr[2]

[1]Institut de Mécanique des Fluides de Toulouse, IMFT, Université de Toulouse, CNRS, Toulouse, 31400, France

[2]Institut de Mécanique des Fluides de Toulouse, IMFT, Université de Toulouse, CNRS, Toulouse, 31400, France

ABSTRACT

Numerical methods generally need analytical solutions as test cases and validations in simplified problems. This work provides Laplace domain explicit analytic solutions for fluid-structure interaction (FSI) water-hammer waves within a pipe. Rather than applying the Transfer Matrix Method (TMM) to the FSI four-equations, it is transposed to the equivalent two-wave propagating problem considered instead. Using the classical wave matrix diagonalisation approach permits to decouple waves propagation, whilst, at the same time, coupling boundary conditions in the diagonal base. This approach permits to provide the transfer matrix for coupled waves boundary conditions so as to obtain a Laplace domain solution for the pressure/stress vector solution. This solution is written in a general framework which can be adapted for general applied boundary conditions for a single pipe. Three sets of boundary conditions are considered as examples and illustrations from solving the inverse Laplace transform of the considered explicit solutions. Consistent results with recently proposed time-domain solutions are found, and a one-to-one mapping between Laplace domain and time domain approaches is also established. This permits to find the discrete spectrum of FSI water-hammer waves mode decomposition from TMM solutions.

INTRODUCTION

Wave propagations in liquid-filled pipe systems is a long standing research topic, having attracted significative research efforts for more than hundred years Allievi (1913); Budny et al. (1991); Burmann (1975); Holmboe and Rouleau (1967); Joukowski (1898); Korteweg (1878); Résal (1876); Skalak (1956). Several review papers can be found on this subject Ferras et al. (2018); Li et al. (2015); Tijsseling (1996) where it is established that the propagation of water-hammer waves is mainly governed by three coupling mechanisms : (i) Poisson coupling, (ii) friction coupling and (iii) junction coupling. (i) is related to the Fluid-Structure-Interactions (FSI) arising at the wave passage from the coupled deformations of the solid in the radial and axial directions (for axi-symmetric "breathing mode" vibrations). (ii) result from the viscous dissipation within the unsteady boundary layer propagating at the wave speed. (iii) results from the applied boundary conditions at pipes ends (for a single pipe). In fact, in the case of unconstrained pipes for which vibrations can arise at frontiers, FSI produce an additional elastic wave distinct from the fluid pressure wave into the pipe. This additional wave also called precursor wave, has a distinct propagating velocity from the fluid pressure one. Furthermore both waves, the fluid pressure wave and the elastic wave are coupled. This coupling is called "Poisson coupling" because it arises from off-diagonal coupling terms proportional to the Poisson coefficient in the general wave equation associated with the pressure/stress vector.

Given the complexity of this coupled waves system, and since the governing equations have been established from several decades (at least without considering friction coupling models), a large part of the literature has considered numerical solutions in time-domain either combining the Method of Characteristic (MOC) Lavooij and Tusseling (1991) or finite volume formulation Daude and Galon (2018) in the fluid with finite elements in the solid. On the other hand, explicit analytical solutions have been developed in more restrained configurations : single pipe, curved pipe El-Raheb (1981), extended blockage Duan et al. (2012) or simple three-like metric graphs Yang et al. (2004a) using the Transfer Matrix Method (TMM) Aliabadi et al. (2020); Keramat and Duan (2021a); Keramat et al. (2021); Li et al. (2002); Liu and Li (2011); Zhang et al. (1999) in

Laplace domain. However, TMM has seldomly been used for comparison and/or validation with time-domain numerical solutions. Since most numerical solutions are provided in time-domain (except those developed in Zhang et al. (1999)), they can indeed hardly benefit from comparison with TMM analytic solutions provided in Laplace domain. This is why a time-domain approach has recently been developed by Bayle and Plouraboué (2023b) using discrete mode decomposition of the FSI water-hammer. FSI effects can indeed significantly alter the high-frequency response of pressure signal Gerosa et al. (2021); Hosoya et al. (2012); Tijsseling et al. (2014) as well as the spectrum of the pressure (frequency shift) in elastic Duan et al. (2013); Henclik (2021); Keramat et al. (2020) as well as viscoelastic pipes Aliabadi et al. (2020); Covas et al. (2004); Gong et al. (2016); Keramat et al. (2021); Meniconi et al. (2012); Soares et al. (2008). The origin of those high-frequency component in the pressure signal comes from the Poisson coupling between the pressure and the longitudinal stress, so that when $\nu_s = 0$, no such phenomenon arise. On the contrary, when $\nu_s > 0$, the fast elastic wave propagation back and forth in the pipe produce high-frequency perturbations in the pressure signal. These high-frequency components of pressure signal can also be useful for other indirect purposes such as leak or defect detection in pipe systems Keramat and Duan (2021b); Keramat et al. (2021); Wang et al. (2021); Zanganeh et al. (2020)., Nevertheless, the link between time-domain analytical solutions and the more established TMM Laplace domain ones has not been discussed yet. In this contribution, we establish and discuss the relation between time-domain discrete mode decomposition solutions and the classical TMM approach. From the derived one-to-one mapping between these two approaches, we discuss how the resulting discrete mode spectrum can also be obtained from TMM solutions. This feature is useful for comparison with numerical predictions in specific configurations. Furthermore, for three specific sets of boundary conditions, the inverse Laplace-transform of the TMM solutions is performed and compared with numerical solutions. The paper is organized as follow. Parameters and governing equations are provided 2 (some additionnal informations are also given in Appendix 4). TMM Laplace domain solution for general boundary conditions are provided in 2. The inverse Laplace transform of these solutions are given in section 2 where the relation with the time-domain

discrete mode decomposition is also discussed. Three specific sets of boundary conditions are then considered in section 3 for which explicit Laplace domain and time domains solutions are obtained and compared with previous numerical solutions of the literature. Finally, convergence of the obtained solutions to mode truncation is finally analyzed in 3.

THEORETICAL FRAMEWORK

This section discusses the Laplace-domain TMM formulation of the water-hammer wave FSI problem for general classes of boundary conditions. TMM is hereby derived for the two-wave FSI propagating problem rather than the classical FSI four -equations one, but these two formulations are exactly equivalent as discussed in Bayle and Plouraboué (2023a). Here we nevertheless consider a less general formulation as the one considered in Bayle and Plouraboué (2023a) where a 2D unknown vector is considered for the pressure-axial stress 2D-vector $\mathbf{P} = (P, \sigma)$ and not a 4D one. This choice comes from considering boundary conditions independent on the velocity, so that, in this case, the general four equation FSI problems boils-down to equivalent and independent two-waves coupled propagation problems. This section discuss the relation between TMM solutions and time-domain analytical solution obtained in Bayle and Plouraboué (2023a) and their discrete spectrum of mode decomposition.

Governing wave-vector equation

Since governing equations and notations are the same as in Bayle and Plouraboué (2023a) there are not repeated here but given in appendix 4. The dimensionless water-hammer FSI wave-equation system with initial condition at rest (Cf (65) and (69) for more details) expressed in the eigenvector base reads

$$\left(\partial_\tau^2 - \mathcal{C}_{\boldsymbol{\mathcal{P}}}^2 \partial_Z^2\right) \boldsymbol{\mathcal{P}} = \mathbf{0} \ \text{, with,} \quad \boldsymbol{\mathcal{P}}(Z,0) = \partial_\tau \boldsymbol{\mathcal{P}}(Z,0) = \mathbf{0}, \tag{1}$$

where the change of basis relations

$$\mathbf{\Pi} = \begin{pmatrix} \frac{2\nu_s \mathcal{D}}{c_-^2 - 1} & \frac{2\nu_s \mathcal{D}}{c_+^2 - 1} \\ 1 & 1 \end{pmatrix}, \quad \mathcal{C}_{\boldsymbol{\mathcal{P}}}^2 = \begin{pmatrix} c_-^2 & 0 \\ 0 & c_+^2 \end{pmatrix} \equiv \mathbf{\Pi} \mathbf{C}_{\mathbf{P}}^2 \mathbf{\Pi}^{-1} \ \text{, and,} \ \boldsymbol{\mathcal{P}} = \mathbf{\Pi}^{-1} \mathbf{P}, \tag{2}$$

have been used. ν_s is the Poisson's modulus and $\mathcal{D}$ the fluid to solid density ratio (provided in (64))

and $c_\pm$ the eigenvalue velocity (68). The pressure-axial stress 2D-vector $\mathbf{P} = (P, \sigma)$ is transformed into a linear combination of those in 2D-vector $\boldsymbol{\mathcal{P}}$ from (2).

The initially coupled pressure/stress wave propagation problem now looks decoupled into two distinct wave propagation modes associated with 2D-vector $\boldsymbol{\mathcal{P}}$. Nevertheless the coupling between $\boldsymbol{\mathcal{P}}$'s components persists from the resulting coupled upstream and downstream boundary conditions associated with $\boldsymbol{\mathcal{P}}$. For the sake of simplification let us introduce four 2×2 matrices $\boldsymbol{\mathcal{N}}$, $\boldsymbol{\mathcal{M}}$, $\boldsymbol{\mathcal{Q}}$, $\boldsymbol{\mathcal{R}}$ and $\boldsymbol{\mathcal{S}}\delta(\tau)$ as a four-dimensional column vector corresponding to the perturbation with respect to the imposed steady-state ($\delta(\tau)$ being Dirac distribution). Boundary conditions can be formally written as a rectangular 8×4 linear system

$$\begin{pmatrix} \boldsymbol{\mathcal{N}} & \boldsymbol{\mathcal{M}} & \mathbf{0} & \mathbf{0} \\ \mathbf{0} & \mathbf{0} & \boldsymbol{\mathcal{Q}} & \boldsymbol{\mathcal{R}} \end{pmatrix}_{8\times4} \cdot \begin{pmatrix} \boldsymbol{\mathcal{P}}(0,\tau) \\ \partial_Z \boldsymbol{\mathcal{P}}(0,\tau) \\ \boldsymbol{\mathcal{P}}(1,\tau) \\ \partial_Z \boldsymbol{\mathcal{P}}(1,\tau) \end{pmatrix}_{8\times1} = \boldsymbol{\mathcal{S}}_{4\times1}\delta(\tau), \tag{3}$$

where $\boldsymbol{\mathcal{S}}\delta(\tau)$ is a source term exciting the system for the impulse response. Specific sets of boundary conditions will hereafter be investigated and corresponding resolution using diagonalised vector wave-equation system (1), are handled in the Laplace domain in section 2.

Laplace resolution of the FSI wave equation

Let us introduce $\mathcal{L}$, the Laplace transform operator, s its Laplace variable and $\tilde{\boldsymbol{\mathcal{P}}}$ the Laplace transform of $\boldsymbol{\mathcal{P}}$:

$$\tilde{\boldsymbol{\mathcal{P}}}(Z,s) = \mathcal{L}\left(\boldsymbol{\mathcal{P}}(Z,t)\right). \tag{4}$$

The Laplace transform of (1) then leads to

$$\left(s^2 - \boldsymbol{\mathcal{C}}^2_{\boldsymbol{\mathcal{P}}}\partial_Z^2\right)\tilde{\boldsymbol{\mathcal{P}}} = \mathbf{0}, \tag{5}$$

$\boldsymbol{\mathcal{C}}_{\boldsymbol{\mathcal{P}}}^2$ being diagonal given (2). A solution can be found for the spatial ODE system leading to

$$\tilde{\boldsymbol{\mathcal{P}}}(Z,s) = \mathbf{E}(Z,s)\tilde{\boldsymbol{\mathcal{P}}}^{\mathcal{D}}(s) + \mathbf{F}(Z,s)\tilde{\boldsymbol{\mathcal{P}}}^{\mathcal{N}}(s), \tag{6}$$

with 2×2 diagonal matrices

$$\mathbf{E}(Z,s) = \begin{pmatrix} \cos\left(\frac{is}{c_-}Z\right) & 0 \\ 0 & \cos\left(\frac{is}{c_+}Z\right) \end{pmatrix}, \quad \mathbf{F}(Z,s) = \begin{pmatrix} \sin\left(\frac{is}{c_-}Z\right) & 0 \\ 0 & \sin\left(\frac{is}{c_+}Z\right) \end{pmatrix}, \tag{7}$$

and $\tilde{\boldsymbol{\mathcal{P}}}^{\mathcal{D}}(s), \tilde{\boldsymbol{\mathcal{P}}}^{\mathcal{N}}(s)$ 2D-vectors yet to be found. $\tilde{\boldsymbol{\mathcal{P}}}^{\mathcal{D}}(s), \tilde{\boldsymbol{\mathcal{P}}}^{\mathcal{N}}(s)$ provide the mode-dependent amplitude of $\tilde{\boldsymbol{\mathcal{P}}}(Z,s)$ respectively associated with the Dirichlet or the Neumann boundary condition imposed at location $Z = 0$. This is a transposition of the transfer matrix method used by Li et al. (2002, 2015); Tijsseling (2003); Zhang et al. (1999), to the wave operator formulation. Combining the expression of (6) and (7) with the Laplace transform of the boundary condition system (3) (into which the Laplace transform of the Dirac distribution $\delta(\tau)$ being equal to one is used), leads to

$$\begin{pmatrix} \tilde{\boldsymbol{\mathcal{P}}}^{\mathcal{D}} \\ \tilde{\boldsymbol{\mathcal{P}}}^{\mathcal{N}} \end{pmatrix}(s) = \boldsymbol{\mathcal{B}}^{-1}(s)\boldsymbol{\mathcal{S}}, \tag{8}$$

with

$$\boldsymbol{\mathcal{B}} = \begin{pmatrix} \boldsymbol{\mathcal{N}} & is\boldsymbol{\mathcal{M}}\boldsymbol{\mathcal{C}}_{\boldsymbol{\mathcal{P}}}^{-1} \\ \boldsymbol{\mathcal{Q}}\mathbf{E}(1) - is\boldsymbol{\mathcal{R}}\boldsymbol{\mathcal{C}}_{\boldsymbol{\mathcal{P}}}^{-1}\mathbf{F}(1) & \boldsymbol{\mathcal{Q}}\mathbf{F}_k(1) + is\boldsymbol{\mathcal{R}}\boldsymbol{\mathcal{C}}_{\boldsymbol{\mathcal{P}}}^{-1}\mathbf{E}(1) \end{pmatrix} \tag{9}$$

In the following development, the inverse of (9) is needed to find $\tilde{\boldsymbol{\mathcal{P}}}$. It is interesting to note that the general solution for arbitrary closure law can easily be deduced from solution (8) by multiplying the hereby considered source term $\boldsymbol{\mathcal{S}}$ by the Laplace transform of the closure law. Alternatively, in time-domain, the general closure law solution are found from a convolution product with the impulse response solution as detailed in Bayle and Plouraboué (2023b). This is why the hereby considered impulse response is interesting to study as a generic solution. By introducing the adjugate matrix of $\boldsymbol{\mathcal{B}}$, namely $\mathbf{adj}\,[\boldsymbol{\mathcal{B}}]$ one can formally see that

$$\boldsymbol{\mathcal{B}}^{-1}(s) = \frac{\mathbf{adj}\,[\boldsymbol{\mathcal{B}}(s)]}{\det \boldsymbol{\mathcal{B}}(s)}, \tag{10}$$

Let us furthermore introduce the two matrices

$$\mathbf{e}_1 = \begin{pmatrix} 1 & 0 & 0 & 0 \\ 0 & 1 & 0 & 0 \end{pmatrix}, \text{ and, } \mathbf{e}_2 = \begin{pmatrix} 0 & 0 & 1 & 0 \\ 0 & 0 & 0 & 1 \end{pmatrix}, \tag{11}$$

vector $\tilde{\boldsymbol{\mathcal{P}}}(s, Z)$ can then be found using (6), (8) and (10) to reach

$$\tilde{\boldsymbol{\mathcal{P}}}(s, Z) = \frac{\boldsymbol{\Phi}(s, Z)}{\det \boldsymbol{\mathcal{B}}(s)}, \tag{12}$$

with

$$\boldsymbol{\Phi}(s, Z) = \left[\mathbf{E}(Z)\mathbf{e}_1 + \mathbf{F}(Z)\mathbf{e}_2\right] \left(\mathbf{adj}\left[\boldsymbol{\mathcal{B}}\right] \boldsymbol{\mathcal{S}}\right). \tag{13}$$

(12)-(13) is the formal solution for the 2D-vector $\tilde{\boldsymbol{\mathcal{P}}}(s, Z)$ in the frequency domain. For specific sets of boundary conditions, this formal solution can be further developed. Nevertheless, there is one salient feature of this solution not yet discussed but of uppermost importance : this solution diverges for specific values of complex variable s. These locations are called the poles of function $\tilde{\boldsymbol{\mathcal{P}}}(s, Z)$. These poles provide deep physical insights since they give the specific natural resonant frequencies of the wave system or, equivalently the specific oscillating modes of the solution in time-domain. The ensemble of these discrete resonant frequencies is called the spectrum of the solution. The reason for this equivalence is found from the inverse Laplace transform which is now discussed. Next section 2 also discusses how to establish the spectrum condition and how it is related to matrix $\boldsymbol{\mathcal{B}}(s)$.

Laplace inversion and time-dependent solution

The pole of (6) are investigated in order to perform the inverse Laplace transform using Cauchy's theorem. Regarding the structure of (6), it immediately appears that the poles are located within the expressions of $\tilde{\boldsymbol{\mathcal{P}}}^{\mathcal{D}}(s)$ and $\tilde{\boldsymbol{\mathcal{P}}}^{\mathcal{N}}(s)$ and, consequently using (8)-(10), within the root of $\det \boldsymbol{\mathcal{B}}(s)$. The adjugate matrix, by definition, does not contribute to the pole set of $\tilde{\boldsymbol{\mathcal{P}}}^{\mathcal{D}}(s)$ and $\tilde{\boldsymbol{\mathcal{P}}}^{\mathcal{N}}(s)$. The condition $\det\left(\boldsymbol{\mathcal{B}}(s)\right) = 0$ is exactly similar to the spectrum condition derived in Bayle and Plouraboué (2023b) and leads to

$$\mathcal{S}_{\mathcal{P}} = \{s \in \mathbb{C} \mid \det \boldsymbol{\mathcal{B}}(s) = 0\}. \tag{14}$$

The resulting transcendental equation for root s_k is specific to each boundary condition set and has to be computed numerically. In the following, three configurations are considered for which, in each case, the root s_k is purely imaginary, i.e.

$$s_k = i\lambda_k \quad \text{, with, } \lambda_k \in \mathbb{R}. \tag{15}$$

(15) provides the one-to-one mapping between the Laplace domain TMM solutions and the time domain ones provided in Bayle and Plouraboué (2023b) because each purely imaginary pole in the frequency domain $s_k = i\lambda_k$ provides the corresponding exponential $\exp(i\lambda_k \tau)$ in the time domain from Cauchy theorem, as now discussed. It is interesting to mention that purely imaginary poles are found for the three specific considered configurations examined in section 3, without stating that it is a general result. This remark goes along with the consideration obtained for the operator spectrum in Bayle and Plouraboué (2023b). The pole set of $\tilde{\boldsymbol{\mathcal{P}}}(Z, s)$, $\mathcal{S}_{\mathcal{P}}$, being found, Cauchy's residue theorem is used to derive a time-domain solution for vector wave problem (1), leading to

$$\boldsymbol{\mathcal{P}}(\tau, Z) = \mathcal{R}_e\left(\sum_{\mathcal{S}_{\mathcal{P}}} \lim_{s \to i\lambda_k} \left((s - i\lambda_k)\frac{\boldsymbol{\Phi}(s, Z)}{\det(\boldsymbol{\mathcal{B}}(s))} e^{s\tau}\right)\right). \tag{16}$$

(16) has been established using a closed countour being a semi-circle of infinite radius in the complex plane, the semi-axis of which being parallel to the imaginary axis with a strictly positive abscissa. This semi-circle has the imaginary axis included in it, and thus all poles Duffy (1994). Then, using the classical Taylor expansion of $\det \boldsymbol{\mathcal{B}}(s)$ at poles $s_k = i\lambda_k$,

$$\boldsymbol{\mathcal{P}}(\tau, Z) = \mathcal{R}_e\left(\sum_{\mathcal{S}_{\mathcal{P}}} \frac{\boldsymbol{\Phi}(i\lambda_k, Z)}{\partial_s \det(\boldsymbol{\mathcal{B}}(i\lambda_k))} e^{i\lambda_k \tau}\right). \tag{17}$$

The previous expression completes the frequency-domain analysis for the time-domain solution of (1). A variety of spatial boundary conditions is then investigated. The associated spectrum will be described and analyzed in detail. Natural frequencies, f_k, found from transcendental spectrum equation roots, s_k, read

$$f_k(Hz) = \frac{s_k c_p}{2\pi i L} = \frac{\lambda_k c_p}{2\pi L}, \tag{18}$$

where L is the pipe's length introduced in §1.

EXPLICIT SOLUTIONS FOR SPECIFIC SETS OF BOUNDARY CONDITIONS

Three sets of boundary conditions are analyzed: (i) the reservoir-pipe-anchored valve system (Fig. **??**a), (ii) the reservoir-pipe-free valve system (Fig. **??**b), (iii) pipe impacted by a rod (Fig. **??**c). Explicit physical parameters associated with these test cases are provided in table 1.

The reservoir-pipe-anchored valve system: : case (i)

In the following configuration depicted in Fig. **??**a, the pipe is supposed perfectly anchored both upstream and downstream. One thereby supposes an homogeneous Neumann condition for the axial stress at $Z = 0$ & $Z = 1$. Furthermore the reservoir impedes any pressure fluctuation upstream which can be interpreted as an homogeneous Dirichlet condition for the pressure field. Finally, downstream, the instantaneous valve closure is modeled with a Dirac distribution $\delta(\tau)$ acting on the axial pressure spatial gradient. The four boundary conditions thereby read

$$P(0,\tau) = 0 \ , \partial_Z P(1,\tau) = \delta(\tau), \quad \partial_Z \sigma(0,\tau) = \partial_Z \sigma(1,\tau) = 0. \tag{19}$$

Invoking the change-of-basis relationships (2) whilst introducing

$$\beta = \frac{c_+}{c_-}\frac{c_-^2 - 1}{c_+^2 - 1}, \tag{20}$$

the boundary condition matrices (3) can then be determined

$$\boldsymbol{\mathcal{N}} = \begin{pmatrix} 1 & \frac{\beta c_-}{c_+} \\ 0 & 0 \end{pmatrix}, \ \boldsymbol{\mathcal{M}} = \begin{pmatrix} 0 & 0 \\ 1 & 1 \end{pmatrix}, \ \boldsymbol{\mathcal{Q}} = \mathbf{0}, \ \boldsymbol{\mathcal{R}} = \boldsymbol{\mathcal{N}} + \boldsymbol{\mathcal{M}}, \ \boldsymbol{\mathcal{S}} = \frac{\left(c_-^2 - 1\right)}{2\nu_s \mathcal{D}} \begin{pmatrix} 0 \\ 0 \\ 1 \\ 0 \end{pmatrix}. \tag{21}$$

The boundary condition matrices are useful to derive an expression for cornerstone matrix $\boldsymbol{\mathcal{B}}$. Invoking the definition of the latter in (9), one finds

$$\boldsymbol{\mathcal{B}} = \begin{pmatrix} 1 & \frac{\beta c_-}{c_+} & 0 & 0 \\ 0 & 0 & \frac{is}{c_-} & \frac{is}{c_+} \\ -is\frac{\sin\left(\frac{is}{c_-}\right)}{c_-} & -is\frac{\beta c_-}{c_+}\frac{\sin\left(\frac{is}{c_+}\right)}{c_+} & is\frac{\cos\left(\frac{is}{c_-}\right)}{c_-} & is\frac{\beta c_-}{c_+}\frac{\cos\left(\frac{is}{c_+}\right)}{c_+} \\ -is\frac{\sin\left(\frac{is}{c_-}\right)}{c_-} & -is\frac{\sin\left(\frac{is}{c_+}\right)}{c_+} & is\frac{\cos\left(\frac{is}{c_-}\right)}{c_-} & is\frac{\cos\left(\frac{is}{c_+}\right)}{c_+} \end{pmatrix}. \tag{22}$$

The determinant of $\boldsymbol{\mathcal{B}}(s)$ can be easily found leading to

$$\det\left(\boldsymbol{\mathcal{B}}(s)\right) = -is^3\frac{c_-\beta - c_+}{c_+^3 c_-}\left[\beta\sin\left(\frac{is}{c_-}\right)\cos\left(\frac{is}{c_+}\right) - \sin\left(\frac{is}{c_+}\right)\cos\left(\frac{is}{c_-}\right)\right], \tag{23}$$

and,

$$\partial_s\det\left(\boldsymbol{\mathcal{B}}(s)\right) = 3\frac{\det\left(\boldsymbol{\mathcal{B}}(s)\right)}{s} + s^3\left(\frac{c_-\beta - c_+}{c_+^2 c_-}\right)^2\left[\frac{c_+\beta - c_-}{c_-\beta - c_+}\cos\left(\frac{is}{c_-}\right)\cos\left(\frac{is}{c_+}\right) - \sin\left(\frac{is}{c_+}\right)\sin\left(\frac{is}{c_-}\right)\right]. \tag{24}$$

Let $s_k = i\lambda_k$, with $\lambda_k \in \mathbb{R}$, be a root of (23). The spectrum associated with the reservoir-pipe-anchored valve configuration arises from λ_k transcendental equation

$$\mathcal{S}_{\mathcal{P}} = \left\{\lambda_k \in \mathbb{R},\ \ \beta\sin\left(\frac{\lambda_k}{c_-}\right)\cos\left(\frac{\lambda_k}{c_+}\right) = \sin\left(\frac{\lambda_k}{c_+}\right)\cos\left(\frac{\lambda_k}{c_-}\right)\right\}. \tag{25}$$

As previously stated (25) exactly matches with the spectrum condition found by Bayle and Plouraboué (2023b) for the very same configuration within a time-domain approach. It remains to establish the expression of $\boldsymbol{\Phi}(s, Z)$ in (13) to provide $\boldsymbol{\mathcal{P}}$ in (17). After considerable algebra efforts (cross-checked with symbolic computation) one finds

$$\mathbf{adj}\left[\boldsymbol{\mathcal{B}}(s)\right]\boldsymbol{\mathcal{S}} = \frac{s^2\left(c_-^2 - 1\right)}{2\nu_s\mathcal{D}}\begin{pmatrix} \frac{\beta}{c_+^2}\left(\cos\left(\frac{is}{c_-}\right) - \cos\left(\frac{is}{c_+}\right)\right) \\ -\frac{1}{c_+c_-}\left(\cos\left(\frac{is}{c_-}\right) - \cos\left(\frac{is}{c_+}\right)\right) \\ \frac{1}{c_+^2}\left(\beta\sin\left(\frac{is}{c_-}\right) - \sin\left(\frac{is}{c_+}\right)\right) \\ -\frac{1}{c_+c_-}\left(\beta\sin\left(\frac{is}{c_-}\right) - \sin\left(\frac{is}{c_+}\right)\right) \end{pmatrix}. \tag{26}$$

At this stage, the solution of the vector wave equation (1) can be expressed in either frequency-domain, combining (23) and (26) in (12), or time-domain, combining (24) and (26) in (17). When evaluating the derivative of the determinant (24) at $s = i\lambda_k$, it turns out to be purely imaginary while the term $\mathbf{adj}\,[\boldsymbol{\mathcal{B}}(s)]\,\boldsymbol{\mathcal{S}}$ in (26) turns out to be real, as matrix $\mathbf{E}(Z,s)$ and $\mathbf{F}(Z,s)$ in (7) do. In other words, when performing the inverse Laplace transform over $\tilde{\boldsymbol{\mathcal{P}}}$ only the temporal sinus mode in (17) contributes and read :

$$\boldsymbol{\mathcal{P}}(Z,\tau) = \frac{\left(c_-^2-1\right)\sum_{\lambda_k\in\mathcal{S}_{\mathcal{P}}}\sin\left(\lambda_k\,\tau\right)}{2\nu_s\,c_+^2\,\mathcal{D}\lambda_k\left(\frac{c_-\beta-c_+}{c_+^2c_-}\right)^2\left[\frac{c_+\beta-c_-}{c_-\beta-c_+}\cos\left(\frac{\lambda_k}{c_-}\right)\cos\left(\frac{\lambda_k}{c_+}\right)-\sin\left(\frac{\lambda_k}{c_+}\right)\sin\left(\frac{\lambda_k}{c_-}\right)\right]}\left[\left(\cos\left(\frac{\lambda_k}{c_-}\right)-\cos\left(\frac{\lambda_k}{c_+}\right)\right)\begin{pmatrix}\beta\cos\left(\frac{\lambda_k Z}{c_-}\right)\\-\frac{c_+}{c_-}\cos\left(\frac{\lambda_k Z}{c_+}\right)\end{pmatrix}+\left(\beta\sin\left(\frac{\lambda_k}{c_-}\right)-\sin\left(\frac{\lambda_k}{c_+}\right)\right)\begin{pmatrix}\sin\left(\frac{\lambda_k Z}{c_-}\right)\\-\frac{c_+}{c_-}\sin\left(\frac{\lambda_k Z}{c_+}\right)\end{pmatrix}\right]. \tag{27}$$

Pressure/stress components can then be deduced from (27) using base-change (2). Figures 1 & 2 illustrate both time-domain solution and its spectrum. It is interesting to observe in Figure 1a the influence of the Poisson coupling coefficient onto the rise of high-frequency components of the pressure signal in the case $\nu_s = 0.3$ (orange continuous curve of Figure 1a). It is important to stress that these high-frequency peaks do not result from some numerical noise nor computational approximation. They result from accurate computation, the underlying physics relying onto the fast bouncing of elastic wave modes into the solid. Since each traveling mode has its own velocity being much faster than the main pressure wave, they manifest themselves into small pressure overshoots the number of which depends on the number of bouncing of each elastic mode each having its own amplitude. The richness of this signal is interesting since it carries important informations about the system's mechanical properties and boundary conditions. The inspection of Figure 2 illustrates how well the hereby presented analytical solutions match with previous numerical results. Also visible in Figure 1a and 2a are small overshoots arising both for Mei and Jing (2016)'s solution as well as ours, at the edge of each wave-front at discrete time $\tau \simeq 2, 4, 6, \ldots$. These small overshoots result from the aliasing effect resulting from high-frequency cutt-off of the Laplace transform as encountered from Nyquist frequency cutt-off in Fourier transforms.

The reservoir-pipe-free valve system : case (ii)

Figure **??**b configuration is now investigated. Upstream, the same conditions (19) are applied, with homogeneous Neumann condition for the axial stress and homogeneous Dirichlet condition for the pressure. Downstream, the static equilibrium of forces at the valve location combined with velocity continuity leads to

$$\alpha(2+\alpha)\sigma(1,\tau) = P(1,\tau), \tag{28}$$

$$\partial_Z P(1,\tau) + \mathcal{D}\partial_Z\sigma(1,\tau) = \delta(\tau). \tag{29}$$

Considering change of basis (2) whilst introducing parameters

$$\kappa_\pm = \mathcal{D} + \frac{2\nu_s \mathcal{D}}{c_\pm^2 - 1}, \tag{30}$$

$$\gamma = \frac{\alpha(2+\alpha) - \frac{2\nu_s \mathcal{D}}{c_+^2 - 1}}{\alpha(2+\alpha) - \frac{2\nu_s \mathcal{D}}{c_-^2 - 1}}, \tag{31}$$

the boundary condition matrices (3) can be found leading to

$$\boldsymbol{\mathcal{N}} = \begin{pmatrix} 1 & \frac{\beta c_-}{c_+} \\ 0 & 0 \end{pmatrix}, \quad \boldsymbol{\mathcal{M}} = \begin{pmatrix} 0 & 0 \\ 1 & 1 \end{pmatrix}, \quad \boldsymbol{\mathcal{Q}} = \begin{pmatrix} 0 & 0 \\ 1 & \gamma \end{pmatrix}, \quad \boldsymbol{\mathcal{R}} = \begin{pmatrix} \kappa_- & \kappa_+ \\ 0 & 0 \end{pmatrix}, \quad \boldsymbol{\mathcal{S}} = \begin{pmatrix} 0 \\ 0 \\ 1 \\ 0 \end{pmatrix}. \tag{32}$$

Using definition (9), $\boldsymbol{\mathcal{B}}$ can be found as

$$\boldsymbol{\mathcal{B}} = \begin{pmatrix} 1 & \frac{\beta c_-}{c_+} & 0 & 0 \\ 0 & 0 & \frac{is}{c_-} & \frac{is}{c_+} \\ -is\frac{\kappa_-}{c_-}\sin\left(\frac{is}{c_-}\right) & -is\frac{\kappa_+}{c_+}\sin\left(\frac{is}{c_+}\right) & is\frac{\kappa_-}{c_-}\cos\left(\frac{is}{c_-}\right) & is\frac{\kappa_+}{c_+}\cos\left(\frac{is}{c_+}\right) \\ \cos\left(\frac{is}{c_-}\right) & \gamma\cos\left(\frac{is}{c_+}\right) & \sin\left(\frac{is}{c_-}\right) & \gamma\sin\left(\frac{is}{c_+}\right) \end{pmatrix} \tag{33}$$

With parametric relation

$$\frac{\kappa_-}{\gamma\kappa_+} = \frac{c_+}{\beta c_-}. \tag{34}$$

The determinant of $\boldsymbol{\mathcal{B}}(s)$ and its derivative with respect to s are

$$\det \boldsymbol{\mathcal{B}}(s) = -\frac{2s^2\beta\kappa_-}{c_+^2} + s^2\frac{\kappa_+}{c_+^2}\left[\beta\cos\left(\frac{is}{c_+}\right)\cos\left(\frac{is}{c_-}\right)\left(1+\left(\frac{\kappa_-}{\kappa_+}\right)^2\right) + \sin\left(\frac{is}{c_+}\right)\sin\left(\frac{is}{c_-}\right)\left(1+\left(\frac{\beta\kappa_-}{\kappa_+}\right)^2\right)\right], \tag{35}$$

$$\partial_s \det \boldsymbol{\mathcal{B}}(s) = is^2\left(\chi_+\sin\left(\frac{is}{c_-}\right)\cos\left(\frac{is}{c_+}\right) + \chi_-\cos\left(\frac{is}{c_-}\right)\sin\left(\frac{is}{c_+}\right)\right) + \frac{2\det\boldsymbol{\mathcal{B}}(s)}{s}, \tag{36}$$

with

$$\chi_\pm = \frac{\kappa_+}{c_+^2}\left(\frac{1}{c_\pm}\left[1+\left(\frac{\beta\kappa_-}{\kappa_+}\right)^2\right] - \frac{\beta}{c_\mp}\left[1+\left(\frac{\kappa_-}{\kappa_+}\right)^2\right]\right), \tag{37}$$

Let $s = i\lambda_k$, with $\lambda_k \in \mathbb{R}$, be a root of (35). The spectrum associated with the reservoir-pipe-free valve configuration is governed by the following λ_k transcendental equation,

$$\beta \cos\left(\frac{\lambda_k}{c_+}\right)\cos\left(\frac{\lambda_k}{c_-}\right)\left(1+\left(\frac{\kappa_-}{\kappa_+}\right)^2\right)+\left(1+\left(\frac{\beta\kappa_-}{\kappa_+}\right)^2\right)\sin\left(\frac{\lambda_k}{c_+}\right)\sin\left(\frac{\lambda_k}{c_-}\right)=\frac{2\kappa_-}{\kappa_+}. \tag{38}$$

Figure 3 illustrate the obtained spectrum (more precisely the first 24 eigenvalues) found from solving the transcendental equation (38) both versus the Poisson coefficient and the dimensionless pipe thickness. These results are interesting for providing explicit values for the natural frequencies when varying the FSI parameter ν_s and the pipe thickness. Here again, the cumbersome determination of $\mathbf{adj}\left(\boldsymbol{\mathcal{B}}(s)\right)\boldsymbol{\mathcal{S}}$ is performed with the help of symbolic computation and leads to

$$\mathbf{adj}\left[\boldsymbol{\mathcal{B}}(s)\right]\boldsymbol{\mathcal{S}} = -is\begin{pmatrix} \frac{\beta}{c_+^2}\left(c_-\sin\left(\frac{is}{c_-}\right)-\gamma c_+\sin\left(\frac{is}{c_+}\right)\right) \\ -\frac{1}{c_-c_+}\left(c_-\sin\left(\frac{is}{c_-}\right)-\gamma c_+\sin\left(\frac{is}{c_+}\right)\right) \\ -\frac{1}{c_+^2}\left(\beta c_-\cos\left(\frac{is}{c_-}\right)-\gamma c_+\cos\left(\frac{is}{c_+}\right)\right) \\ \frac{1}{c_-c_+}\left(\beta c_-\cos\left(\frac{is}{c_-}\right)-\gamma c_+\cos\left(\frac{is}{c_+}\right)\right) \end{pmatrix}. \tag{39}$$

From this, the solution of the vector wave equation (1) can either be expressed in frequency-domain, combining (35) and (39) in (12), or in time-domain, combining (36) and (39) in (17). In time domain, the solution reads

$$\begin{aligned}\boldsymbol{\mathcal{P}}(Z,\tau) = &-\sum_{\lambda_k\in\mathcal{S}_\mathcal{P}}\frac{\left(c_-\sin\left(\frac{\lambda_k}{c_-}\right)-\gamma c_+\sin\left(\frac{\lambda_k}{c_+}\right)\right)\begin{pmatrix}\beta\cos\left(\frac{\lambda_k Z}{c_-}\right)\\ -\frac{c_+}{c_-}\cos\left(\frac{\lambda_k Z}{c_+}\right)\end{pmatrix}}{\lambda_k c_+^2\left(\chi_+\sin\left(\frac{\lambda_k}{c_-}\right)\cos\left(\frac{\lambda_k}{c_+}\right)+\chi_-\cos\left(\frac{\lambda_k}{c_-}\right)\sin\left(\frac{\lambda_k}{c_+}\right)\right)}\sin\left(\lambda_k\tau\right)\\ &+\sum_{\lambda_k\in\mathcal{S}_\mathcal{P}}\frac{\left(\beta c_-\cos\left(\frac{\lambda_k}{c_-}\right)-\gamma c_+\cos\left(\frac{\lambda_k}{c_+}\right)\right)\begin{pmatrix}\sin\left(\frac{\lambda_k Z}{c_-}\right)\\ -\frac{c_+}{c_-}\sin\left(\frac{\lambda_k Z}{c_+}\right)\end{pmatrix}}{\lambda_k c_+^2\left(\chi_+\sin\left(\frac{\lambda_k}{c_-}\right)\cos\left(\frac{\lambda_k}{c_+}\right)+\chi_-\cos\left(\frac{\lambda_k}{c_-}\right)\sin\left(\frac{\lambda_k}{c_+}\right)\right)}\sin\left(\lambda_k\tau\right).\end{aligned} \tag{40}$$

Here again, pressure/stress components can then be obtained from (40) using base-change (2). Figure 4 illustrates the time domain solution (40), with again very good comparison with previous numerical results.

The impact induced water hammer : case (iii)

The third configuration of Figure **??**c is now investigated associated with the over-pressure produced from the impact of a steel rod on a closed liquid-filled pipe system. This ingenious experiment was designed by Vardy and Fan (1986) to reveal intrinsic FSI coupling occurring in liquid-filled pipes while minimizing external disturbing contributions. This system has been analytically investigated in Li et al. (2002, 2003). At the upstream pipe end, a steel rod impacts the pipe sleeve producing an over-stress which propagates within the fluid/solid system. While the impact time of the rod over the upstream sleeve is supposed negligible, one nevertheless considers the sleeve's inertia, as illustrated in Fig. 10 of Tijsseling and Vardy (1996) which shows measured "impact times".

The dynamic equilibrium of forces along with the velocity continuity at both pipe's upstream and downstream ends leads to

$$m_0 \mathcal{D} \partial_Z \sigma_{zz}(0,\tau) = \mathcal{F}_r \delta(\tau) + \alpha(2+\alpha)\sigma_{zz}(0,\tau) - P(0,\tau), \tag{41}$$

$$\mathcal{D} \partial_Z \sigma_{zz}(0,\tau) + \partial_Z P(0,\tau) = 0, \tag{42}$$

$$-m_L \mathcal{D} \partial_Z \sigma_{zz}(1,\tau) = \alpha(2+\alpha)\sigma_{zz}(1,\tau) - P(1,\tau), \tag{43}$$

$$\mathcal{D} \partial_Z \sigma_{zz}(1,\tau) + \partial_Z P(1,\tau) = 0. \tag{44}$$

where

$$m_{\substack{0\\L}} = \frac{M_{\substack{0\\L}}}{\pi \rho_f R^2 L}, \tag{45}$$

$$\mathcal{F}_r = \frac{F_{rod}}{\pi \rho_f c_p V_{rod} R^2}. \tag{46}$$

Considering change of basis relations (2) and introducing parameters

$$\eta_{\substack{0\\L}} = \frac{m_{\substack{0\\L}} \mathcal{D}}{\alpha(2+\alpha) - \frac{2\nu_s \mathcal{D}}{c_=^2 - 1}}, \tag{47}$$

$$\mathcal{F} = \frac{\mathcal{F}_r}{\alpha(2+\alpha) - \frac{2\nu_s \mathcal{D}}{c_=^2 - 1}}, \tag{48}$$

the boundary conditions matrices (3) can be determined

$$\boldsymbol{\mathcal{N}} = -\begin{pmatrix} 0 & 0 \\ 1 & \gamma \end{pmatrix}, \quad \boldsymbol{\mathcal{M}} = \begin{pmatrix} \kappa_- & \kappa_+ \\ \eta_0 & \eta_0 \end{pmatrix}, \quad \boldsymbol{\mathcal{Q}} = -\boldsymbol{\mathcal{N}}, \quad \boldsymbol{\mathcal{R}} = \begin{pmatrix} \kappa_- & \kappa_+ \\ \eta_L & \eta_L \end{pmatrix}, \quad \boldsymbol{\mathcal{S}} = \begin{pmatrix} 0 \\ \mathcal{F} \\ 0 \\ 0 \end{pmatrix}. \tag{49}$$

Cornerstone matrix $\boldsymbol{\mathcal{B}}$ can now be evaluated using (9)

$$\boldsymbol{\mathcal{B}} = \begin{pmatrix} 0 & 0 & is\frac{\kappa_-}{c_-} & is\frac{\kappa_+}{c_+} \\ -1 & -\gamma & \frac{is\eta_0}{c_-} & \frac{is\eta_0}{c_+} \\ -is\frac{\kappa_-\sin\left(\frac{is}{c_-}\right)}{c_-} & -is\frac{\kappa_+\sin\left(\frac{is}{c_+}\right)}{c_+} & is\frac{\kappa_-\cos\left(\frac{is}{c_-}\right)}{c_-} & is\frac{\kappa_+\cos\left(\frac{is}{c_+}\right)}{c_+} \\ \mathcal{B}_{41}(s) & \mathcal{B}_{42}(s) & \mathcal{B}_{43}(s) & \mathcal{B}_{44}(s) \end{pmatrix}, \tag{50}$$

with

$$\mathcal{B}_{41}(s) = \cos\left(\frac{is}{c_-}\right) - \frac{is\eta_L}{c_-}\sin\left(\frac{is}{c_-}\right), \quad \mathcal{B}_{42}(s) = \gamma\cos\left(\tfrac{is}{c_+}\right) - \tfrac{is\eta_L}{c_+}\sin\left(\tfrac{is}{c_+}\right), \tag{51}$$

$$\mathcal{B}_{43}(s) = \sin\left(\frac{is}{c_-}\right) + \frac{is\eta_L}{c_-}\cos\left(\frac{is}{c_-}\right), \quad \mathcal{B}_{44}(s) = \gamma\sin\left(\tfrac{is}{c_+}\right) + \tfrac{is\eta_L}{c_+}\cos\left(\tfrac{is}{c_+}\right). \tag{52}$$

Introducing parameter ψ as

$$\psi = \beta\left(\frac{\kappa_-}{\kappa_+}\right)^2, \tag{53}$$

the determinant of $\boldsymbol{\mathcal{B}}(s)$ can be evaluated

$$\begin{aligned} \det\boldsymbol{\mathcal{B}}(s) \;=\; & s^2\frac{\eta_0\eta_L\left(\kappa_- - \kappa_+\right)^2 s^2 + c_-^2\kappa_+^2\left(1+\psi^2\right)}{c_-^2c_+^2}\sin\left(\frac{is}{c_-}\right)\sin\left(\frac{is}{c_+}\right) \\ & + is^3\frac{\kappa_+\left(\kappa_- - \kappa_+\right)\left(\eta_0+\eta_L\right)}{c_-c_+^2}\left(\psi\cos\left(\frac{is}{c_+}\right)\sin\left(\frac{is}{c_-}\right) - \cos\left(\frac{is}{c_-}\right)\sin\left(\frac{is}{c_+}\right)\right) + 2s^2\frac{\psi\kappa_+^2}{c_+^2}\left(\cos\left(\frac{is}{c_-}\right)\cos\left(\frac{is}{c_+}\right) - 1\right), \end{aligned} \tag{54}$$

so does its derivative

$$\partial_s \det \boldsymbol{\mathcal{B}}(s) = \frac{2\det \boldsymbol{\mathcal{B}}(s)}{s} - s^3 \cos\left(\frac{is}{c_-}\right)\cos\left(\frac{is}{c_+}\right)\frac{\kappa_+(\kappa_- - \kappa_+)(\eta_0+\eta_L)}{c_- c_+^2}\left[\frac{\psi}{c_-} - \frac{1}{c_+}\right]$$
$$+ \frac{is^2}{c_- c_+^2}\cos\left(\frac{is}{c_+}\right)\sin\left(\frac{is}{c_-}\right)\left[\psi\kappa_+\left((\kappa_- - \kappa_+)(\eta_0+\eta_L) - 2\kappa_+\right) + \frac{\eta_0\eta_L(\kappa_- - \kappa_+)^2 s^2 + c_-^2\kappa_+^2(1+\psi^2)}{c_- c_+}\right]$$
$$+ \frac{is^2}{c_+^2}\cos\left(\frac{is}{c_-}\right)\sin\left(\frac{is}{c_+}\right)\left[\frac{\eta_0\eta_L(\kappa_- - \kappa_+)^2 s^2 + c_-^2\kappa_+^2(1+\psi^2)}{c_-^3} - \kappa_+\left(\frac{(\kappa_- - \kappa_+)(\eta_0+\eta_L)}{c_-} + \frac{2\psi\kappa_+}{c_+}\right)\right]$$
$$+ s^3 \sin\left(\frac{is}{c_-}\right)\sin\left(\frac{is}{c_+}\right)\frac{\kappa_- - \kappa_+}{c_- c_+^2}\left[\frac{2\eta_0\eta_L(\kappa_- - \kappa_+)}{c_-} - \kappa_+(\eta_0+\eta_L)\left(\frac{1}{c_-} - \frac{\psi}{c_+}\right)\right] \quad (55)$$

Furthermore $\mathbf{adj}\,[\boldsymbol{\mathcal{B}}(s)]\,\boldsymbol{\mathcal{S}}$ is evaluated and reads

$$\mathbf{adj}\,[\boldsymbol{\mathcal{B}}(s)]\,\boldsymbol{\mathcal{S}} = -s^2\mathcal{F}\begin{pmatrix} \frac{\left[-is\eta_L\kappa_+(\kappa_- - \kappa_+)\sin\left(\frac{is}{c_+}\right) + c_-\kappa_+^2\psi\cos\left(\frac{is}{c_+}\right)\right]\cos\left(\frac{is}{c_-}\right) + c_-\kappa_+^2\left[\sin\left(\frac{is}{c_-}\right)\sin\left(\frac{is}{c_+}\right) - \psi\right]}{c_- c_+^2} \\ \frac{\kappa_-}{\kappa_+}\frac{\left[is\eta_L\kappa_+(\kappa_- - \kappa_+)\sin\left(\frac{is}{c_-}\right) + c_-\kappa_+^2\cos\left(\frac{is}{c_-}\right)\right]\cos\left(\frac{is}{c_+}\right) + c_-\kappa_+^2\left[\sin\left(\frac{is}{c_-}\right)\sin\left(\frac{is}{c_+}\right)\psi - 1\right]}{c_+ c_-^2} \\ \frac{\left[-is\eta_L\kappa_+(\kappa_- - \kappa_+)\sin\left(\frac{is}{c_+}\right) + c_-\kappa_+^2\psi\cos\left(\frac{is}{c_+}\right)\right]\sin\left(\frac{is}{c_-}\right) - c_-\kappa_+^2\sin\left(\frac{is}{c_+}\right)\cos\left(\frac{is}{c_-}\right)}{c_- c_+^2} \\ -\frac{\kappa_-}{\kappa_+}\frac{\left[-is\eta_L\kappa_+(\kappa_- - \kappa_+)\sin\left(\frac{is}{c_+}\right) + c_-\kappa_+^2\psi\cos\left(\frac{is}{c_+}\right)\right]\sin\left(\frac{is}{c_-}\right) - c_-\kappa_+^2\sin\left(\frac{is}{c_+}\right)\cos\left(\frac{is}{c_-}\right)}{c_-^2 c_+} \end{pmatrix}. \quad (56)$$

In time domain, the transformed pressure/stress 2D vector $\boldsymbol{\mathcal{P}}$

$$\boldsymbol{\mathcal{P}}(Z,\tau) = -\sum_{\lambda_k \in \mathcal{S}_{\mathcal{P}}} \frac{\lambda_k^2\mathcal{F}}{\partial_s \det \boldsymbol{\mathcal{B}}(i\lambda_k)} \sin\lambda_k\tau\,\boldsymbol{\mathcal{P}}'(Z) \quad (57)$$

where $\partial_s \det \boldsymbol{\mathcal{B}}(i\lambda_k)$ is given by (55) and vector $\boldsymbol{\mathcal{P}}'(Z)$ components are

$$\boldsymbol{\mathcal{P}}'(Z) = \begin{pmatrix} \lambda_k\eta_L\kappa_+(\kappa_+ - \kappa_-)\sin\frac{\lambda_k}{c_+}\cos\frac{\lambda_k(Z-1)}{c_-} - (\frac{\kappa_+}{c_+})^2\left(\psi\cos\frac{\lambda_k}{c_+}\cos\frac{\lambda_k(Z-1)}{c_-} + \sin\frac{\lambda_k}{c_+}\sin\frac{\lambda_k(Z-1)}{c_-} + \psi\cos\frac{\lambda_k Z}{c_-}\right) \\ \frac{\kappa_-}{c_+ c_-^2\kappa_+}[\lambda_k\eta_L\kappa_+(\kappa_- - \kappa_+)\sin\frac{\lambda_k}{c_-}\cos\frac{\lambda_k(Z-1)}{c_+} + c_-\kappa_+^2\left(-\psi\sin\frac{\lambda_k}{c_-}\sin\frac{\lambda_k(Z-1)}{c_+} + \cos\frac{\lambda_k}{c_-}\cos\frac{\lambda_k(Z-1)}{c_+} - \cos\frac{\lambda_k Z}{c_+}\right)] \end{pmatrix} \quad (58)$$

Finally, as previously noted the pressure and longitudinal stress components can be found from applying the base-change matrix $\boldsymbol{\Pi}$ defined in (2) to vector $\boldsymbol{\mathcal{P}}(Z,\tau)$. The spectrum associated with this configuration is found using (55) from solving transcendental equation $\det \boldsymbol{\mathcal{B}}(s) = 0$. The spectrum numerical evaluation is carried-out to investigate the shift of natural frequencies caused by the geometrical parameter α in figure 5b for a wide range of dimensionless pipe thickness parameter α. The natural frequencies are also compared in Fig. 5a with the ones found by Zhang et al. (1999). Again a very good match is found from comparing

analytical results with the natural frequency of the previous numerical simulations. This results also illustrates the importance of considering the sleeve masses in such systems. The fourth and eighth frequencies are considerably affected by the oscillations of the pipe's end masses.

Modal convergence analysis

Even if the hereby presented solutions are analytical, they can only be numerically approximated since the spectrum's eigenvalues needs to be numerically computed and a finite number of node can only be evaluated, out of the theoretically infinite series. This is why this section investigates how much mode are needed in order to produce a sensible approximation of the exact solution. The mode truncation convergence of our analytical solution is checked by evaluating the quadratic error E

$$E = \frac{1}{N_Z N_\tau} \int_0^1 \int_0^{\tau=5} \left(\mathcal{P}_{M_{tr}}(z,t) - \mathcal{P}_{ref}(z,t)\right)^2 dzdt, \tag{59}$$

where $(N_Z, N_\tau) \equiv (1000, 5000)$ are the space and time numerical uniform grid point number whereas $\mathcal{P}_{ref}(Z,\tau)$ is a reference solution with very-high mode truncation (2000 modes). For each configuration analyzed the analytical solution is truncated to M_{tr} modes (with $M_{tr} \ll 2000$). Figure 6 shows a linear convergence of mode truncation, i.e the $\mathcal{L}_2$-norm of the error E decays as $E \sim M_{tr}^{-1}$. Furthermore figure 6 indicates that both in case (i) and (ii), the $\mathcal{L}_2$-norm can be as small as 2.10^{-9} when taking only the first hundred modes. This illustrates that albeit high frequencies are needed in order to describe the sharp time variation of the pressure solution, they are not contributing much for most of the pressure signal shape. Furthermore, in practice, since any real "impact time" has a finite time decay, not every high frequency mode can be excited, providing physical relevance to mode truncation.

SUMMARY AND CONCLUSION

The paper considers analytical solutions for FSI wave propagation in liquid-filled pipes using TMM method in frequency-domain. Transposing the TMM method to the 2×2 wave system associated with the pressure/stress coupled unknown, the formal solution in frequency-domain is provided for general (linear) sets of boundary conditions. The poles of this frequency-domain solutions give the natural vibrating frequencies of the system, i.e the discrete spectrum of the vibrating modes. The spectrum has been found associated with the zeros of the determinant of a transfer matrix (denoted $\mathcal{B}$) which encapsulates both FSI and boundary conditions couplings. The resulting spectrum is found consistent with the one found

previously using time-domain analysis. Considering three sets of boundary conditions, the diagonalized pressure-stress wave equation has been analyzed by a frequency-domain Laplace transform approach. For all configurations investigated, an explicit transcendental spectrum equation has been obtained. A detailed analysis of the spectrum variations versus constitutive parameters , i.e the Poisson modulus or the pipe's thickness radius ratio α) has then been carried out. The determined natural frequencies were successfully compared with previous contributions found in the literature. For the pipe-reservoir-valve (free or not) system, a straightforward time dependent solution has been derived and compared to numerical benchmarks. The modal convergence of the time dependent solutions have been analyzed showing a good convergence to mode truncation. We hope that these analytical solutions providing the explicit natural frequency spectrum dependence upon mechanical and geometrical parameters can be useful for testing and validating FSI numerical methods. Also, this contribution provides a one-to-one mapping between frequency-domain solutions and time-domain ones. It should then permit to find explicit natural frequency spectrum using TMM method in frequency-domain in more complex configurations.

Appendix

Notations regarding the pipe geometry and mechanical properties are given in this appendix. A cylindrical tube having inner radius R_0, wall thickness e, length L, is considered so that the dimensionless pipe thickness α can be defined as

$$\alpha = \frac{e}{R_0}. \tag{60}$$

The tube is entirely filled with a fluid having density ρ_f, bulk modulus $\mathcal{K}_f$. The elastic solid response is associated with Young's modulus E, Poisson's modulus ν_s, and density ρ_s. Tijsseling (2007) derived the classical pulse wave speed within the fluid, c_p, distinct from the elastic pulse wave speed within the solid, c_s

$$c_p^2 = \frac{1}{\rho_f} \frac{1}{\frac{1}{\mathcal{K}_f} + \frac{2}{\alpha E}\left(\frac{2(1-\nu_s^2)}{2+\alpha} + \alpha(1+\nu_s)\right)}, \quad c_s^2 = \frac{E}{\rho_s}, \tag{61}$$

their respective ratio being

$$C_s = \frac{c_s}{c_p}. \tag{62}$$

The perturbed fluid pressure P^*, and axial solid stress σ^* (in the following we use σ^* to denote the longitudinal stress component σ_{zz}^*), are re-scaled by the Joukowski (1898)'s over-pressure, i.e. $O\left(\rho_f c_p W_0\right)$ where W_0 is

the flow variation applied within the pipes, so that their dimensionless counterparts are denoted

$$P = \frac{P^*}{\rho_f c_p W_0} \text{ , and, } \sigma = \frac{\sigma^*}{\rho_f c_p W_0}. \tag{63}$$

The physical time t is furthermore re-scaled with respect to the fluid acoustic advective time scale, i.e. $\tau = t\frac{L}{c_p}$, whereas the axial coordinate is non-dimensionalysed by the pipe's length, i.e. $Z = z/L$. Finally, the dimensionless density ratio is introduced

$$\mathcal{D} = \frac{\rho_f}{\rho_s}. \tag{64}$$

The derivation of the wave-vector equation governing the space-time distribution of the dimensionless perturbed pressure P and dimensionless axial stress σ has been provided in Bayle and Plouraboué (2023b) so that it is not repeated here. It results in the following wave-operator acting on the pressure/stress 2D-vector:

$$\left(\partial_\tau^2 - \mathbf{C}_\mathbf{P}^2 \partial_Z^2\right) \mathbf{P} = \mathbf{0}, \tag{65}$$

where

$$\mathbf{C}_\mathbf{P}^2 = \begin{pmatrix} 1 & 2\nu_s\mathcal{D} \\ \frac{2\nu_s}{\alpha(2+\alpha)} & \frac{4\nu_s^2\mathcal{D}}{\alpha(2+\alpha)} + C_s^2 \end{pmatrix} \text{ , and, } \mathbf{P} = \begin{pmatrix} P \\ \sigma \end{pmatrix}. \tag{66}$$

As mentionned in the introduction, it is interesting to notice that the off-diagonal terms of matrix $\mathbf{C}_\mathbf{P}^2$ are proportional to the Poisson coefficient ν_s so that the fluid pressure and the solid stress decouple as $\nu_s \to 0$. Furthermore, as $\nu_s \to 0$ the remaining diagonal terms are 1 and C_s^2, the two eigenvalues of the resulting diagonal matrix. These eigenvalues are providing the two distinct wave-velocities of the uncoupled limit: 1 which is the dimensionless pressure pulse velocity c_p whereas C_s^2 is the dimensionless elastic wave solid one. When $\nu_s \neq 0$ the eigenvalues of matrix $\mathbf{C}_\mathbf{P}^2$ provide the velocities of the coupled system. The vector homogeneous wave-equation resolution will be handled within the eigenvectors basis of $\mathbf{C}_\mathbf{P}^2$ as in Zhang et al. (1999). The eigenvalues of $\mathbf{C}_\mathbf{P}^2$, denoted $c_\pm^2 > 0$, associated with diagonalized matrix $\boldsymbol{\mathcal{C}}_\boldsymbol{\mathcal{P}}^2$ correspond to the wave speed mode propagation. They are the solution of the following polynomial characteristic problem

$$c_\pm^4 - \left[1 + C_s^2 + \frac{4\nu_s^2\mathcal{D}}{\alpha(2+\alpha)}\right] c_\pm^2 + C_s^2 = 0, \tag{67}$$

the solutions of which are

$$c_{\pm}^2 = \frac{1 + C_s^2 + \frac{4\nu_s^2 \mathcal{D}}{\alpha(2+\alpha)} \pm \sqrt{\left(1 + C_s^2 + \frac{4\nu_s^2 \mathcal{D}}{\alpha(2+\alpha)}\right)^2 - 4C_s^2}}{2}. \tag{68}$$

The fluid pressure and the axial solid stress as well as their respective time-derivatives will be assumed initially at rest so that

$$\mathbf{P}(Z,0) = \mathbf{0} \ , \partial_\tau \mathbf{P}(Z,0) = \mathbf{0}. \tag{69}$$

Data Availability Statement

- All data, models, and code generated or used during the study appear in the submitted article.

Acknowledgments

This work is under a CC-BY 4.0 licence. This work was supported by the collaborative ANRT Grant CIFRE 2019/1453 co-funded by SETOM, dedicated society of Veolia for the public drinking water service of Toulouse Métropole operating under the brand Eau de Toulouse Métropole. We thanks the referees and the editor for their handling of the editorial process.

The authors have no competing interests to declare.

REFERENCES

Aliabadi, H. K., Ahmadi, A., and Keramat, A. (2020). "Frequency response of water hammer with fluid-structure interaction in a viscoelastic pipe." *Mech Syst Signal Process*, 144, 106848.

Allievi, L. (1913). "Teoria del colpo d'ariete, atti collegio ing. arch.(english translation by Halmos E.E. 1929), The theory of waterhammer." *Trans. ASME*.

Bayle, A. and Plouraboué, F. (2023a). "Low–mach number asymptotic analysis of Fluid Structure Interaction (FSI) pressure waves inside an elastic tube." *Eur. J. Mech. B Fluids*, 101, 59–88.

Bayle, A. and Plouraboué, F. (2023b). "Spectral properties of Fluid Structure Interaction pressure/stress waves in liquid filled pipes." *Wave Motion*, 116, 103081.

353 Budny, D. D., Wiggert, D. C., and Hatfield, F. J. (1991). "The Influence of Structural Damping on Internal
354 Pressure During a Transient Pipe Flow." *J. Fluids Eng.*, 113(3), 424–429.

355 Burmann, W. (1975). "Water hammer in coaxial pipe systems." *J. Hydraul. Eng.*, 101(6), 699–715.

356 Covas, D., Stoianov, I., Ramos, H., G., N., Maksimović, C., and Butler, D. (2004). "Water hammer in
357 pressurized polyethylene pipes: conceptual model and experimental analysis." *Urban Water J.*, 1(2),
358 177–197.

359 Daude, F. and Galon, P. (2018). "A finite-volume approach for compressible single- and two-phase flows in
360 flexible pipelines with fluid-structure interaction." *J. Comput. Phys*, 362, 375–408.

361 Duan, H., Lee, P. J., Ghidaoui, M. S., and Tung, Y. (2012). "Extended Blockage Detection in Pipelines by
362 Using the System Frequency Response Analysis." *J. Water Resour. Plan. Manag.*, 138(1), 55–62.

363 Duan, H.-F., Lee, P. J., Kashima, A., Lu, J., Ghidaoui, M. S., and Tung, Y. (2013). "Extended Block-
364 age Detection in Pipes Using the System Frequency Response: Analytical Analysis and Experimental
365 Verification." *J. Hydraul. Eng.*, 139(7), 763–771.

366 Duffy, D. G. (1994). *Transform methods for solving partial differential equations*. CRC press.

367 El-Raheb, M. (1981). "Vibrations of three-dimensional pipe systems with acoustic coupling." *J. Sound Vib.*,
368 78(1), 39–67.

369 Ferras, D., Manso, P., Schleiss, A., and Covas, D. (2018). "One-dimensional fluid-structure interaction
370 models in pressurized fluid-filled pipes: A review." *Appl. Sci.*, 8(10), 1844.

371 Gerosa, R. M., Osório, J. H., Lopez-Cortes, D., Cordeiro, C. M. B., and De Matos, C. J. S. (2021).
372 "Distributed Pressure Sensing Using an Embedded-Core Capillary Fiber and Optical Frequency Domain
373 Reflectometry." *IEEE Sensors Journal*, 21(1), 360–365.

374 Gong, J., Zecchin, A. C., Lambert, M. F., and Simpson, A. R. (2016). "Determination of the Creep Function
375 of Viscoelastic Pipelines Using System Resonant Frequencies with Hydraulic Transient Analysis." *J.*
376 *Hydraul. Eng.*, 142(9), 04016023.

Henclik, S. (2021). "Application of the shock response spectrum method to severity assessment of water hammer loads." *Mech Syst Signal Process*, 157.

Holmboe, E. L. and Rouleau, W. T. (1967). "The Effect of Viscous Shear on Transients in Liquid Lines." *J. Basic Eng.*, 89(1), 174–180.

Hosoya, N., Kajiwara, I., and Hosokawa, T. (2012). "Vibration testing based on impulse response excited by pulsed-laser ablation: Measurement of frequency response function with detection-free input." *J. Sound Vib.*, 331(6), 1355–1365.

Joukowski, N. (1898). "Memoirs of the imperial academy society of st. petersburg [Über den hydraulischen stoss in wasserleitungsröhren].

Keramat, A. and Duan, H. F. (2021a). "Spectral based pipeline leak detection using a single spatial measurement." *Mech Syst Signal Process*, 161, 107940.

Keramat, A. and Duan, H.-F. (2021b). "Spectral based pipeline leak detection using a single spatial measurement." *Mech Syst Signal Process*, 161, 107940.

Keramat, A., Fathi-Moghadam, M., Zanganeh, R., Rahmanshahi, M., Tijsseling, A. S., and Jabbari, E. (2020). "Experimental investigation of transients-induced fluid–structure interaction in a pipeline with multiple-axial supports." *J Fluids Struct*, 93, 102848.

Keramat, A., Karney, B., Ghidaoui, M. S., and Wang, X. (2021). "Transient-based leak detection in the frequency domain considering fluid-structure interaction and viscoelasticity." *Mech Syst Signal Process*, 153, 107500.

Korteweg, D. (1878). "Ueber die fortpflanzungsgeschwindigkeit des schalles in elastischen röhren (on the speed of sound propagation in elastic tubes)." *Ann. Phys.*, 241(12), 525–542.

Lavooij, C. and Tusseling, A. (1991). "Fluid-structure interaction in liquid-filled piping systems." *J. Fluids Struct.*, 5(5), 573–595.

Li, Q., Yang, K., Zhang, L., and Zhang, N. (2002). "Frequency domain analysis of fluid–structure interaction in liquid-filled pipe systems by transfer matrix method." *INT J MECH SCI*, 44, 2067–2087.

Li, Q. S., Yang, K., and Zhang, L. (2003). "Analytical Solution for Fluid-Structure Interaction in Liquid-Filled Pipes Subjected to Impact-Induced Water Hammer." *Journal of Engineering Mechanics*, 129(12), 1408–1417.

Li, S., Karney, B. W., and Liu, G. (2015). "FSI research in pipeline systems – A review of the literature." *J Fluids Struct*, 57, 277–297.

Liu, G. and Li, Y. (2011). "Vibration analysis of liquid-filled pipelines with elastic constraints." *J. Sound Vib.*, 330(13), 3166–3181.

Mei, C. C. and Jing, H. (2016). "Pressure and wall shear stress in blood hammer - Analytical theory." *Mathematical Biosciences*, 280, 62–70.

Meniconi, S., Brunone, B., and Ferrante, M. (2012). "Water-hammer pressure waves interaction at cross-section changes in series in viscoelastic pipes." *J Fluids Struct*, 33, 44–58.

Résal, H. (1876). "Note sur les petits mouvements d'un fluide incompressible dans un tuyau élastique.." *Journal de Mathematiques Pures et Appliquées*, 2, 342–344.

Skalak, R. (1956). "An extension of the theory of waterhammer." *Transactions of the ASME*, 78, 105–116.

Soares, A. K., Covas, D., and Reis, L. F. (2008). "Analysis of PVC Pipe-Wall Viscoelasticity during Water Hammer." *J. Hydraul. Eng.*, 134(9).

Tijsseling, A. (2007). "Water hammer with fluid-structure interaction in thick-walled pipes." *Comput Struct*, 85, 844–851.

Tijsseling, A. S. (1996). "Fluid structure interaction in liquid filled pipe systems: a review." *J Fluids Struct*, 10(2), 109–146.

Tijsseling, A. S. (2003). "Exact solution of linear hyperbolic four-equation system in axial liquid-pipe vibration." *J Fluids Struct*, 18(2), 179–196.

Tijsseling, A. S., Hou, Q., Svingen, B., and Bergant, A. (2014). "Acoustic resonance experiments in a reservoir - pipeline - orifice system." *Proceedings of the asme pressure vessels and piping conference -*

426 *2013, vol 4: fluid-structure interaction*, A. Tijsseling, ed., ASME, Pressure Vessels & Pip Div. ASME
427 Pressure Vessels and Piping Conference (PVP-2013), Paris, FRANCE, JUL 14-18, 2013.

428 Tijsseling, A. S. and Vardy, A. E. (1996). "Characterization of the Ionic Wind Induced by a Sine DBD
429 Actuator Used for Laminar-to-Turbulent Transition Delay." *Proc. of the 7th Int. Conf. on Pressure Surges*
430 *and Fluid Transients in Pipelines and Open Channels*, Harrogate, UK, 363–383.

431 Vardy, A. and Fan, D. (1986). "Water hammer in a closed tube." *Proceedings of the Fifth International*
432 *Conference on Pressure Surge, BHRA*, Hanover, Germany, 123–137.

433 Wang, X., Camino, G. A., Che, T.-C., and Ghidaoui, M. S. (2021). "Factorized wave propagation model in
434 tree-type pipe networks and its application to leak localization." *Mech Syst Signal Process*, 147, 107116.

435 Yang, K., Li, Q. S., and Zhang, L. (2004a). "Longitudinal vibration analysis of multi-span liquid-filled
436 pipelines with rigid constraints." *J. Sound Vib.*, 273(1), 125–147.

437 Yang, K., Li, Q. S., and Zhang, L. (2004b). "Longitudinal vibration analysis of multi-span liquid-filled
438 pipelines with rigid constraints." *J. Sound Vib.*, 273(1), 125–147.

439 Zanganeh, R., Jabbari, E., Tijsseling, A., and Keramat, A. (2020). "Fluid-Structure Interaction in Transient-
440 Based Extended Defect Detection of Pipe Walls." *J. Hydraul. Eng.*, 146(4), 04020015.

441 Zhang, L., Tijsseling, A., and Vardy, A. (1999). "FSI analysis of liquid-filled pipes." *J. Sound Vib.*, 224,
442 69–99.

List of Tables

[Physical properties and configuration for case (i) & (ii)]

Anchored and free valves (i) & (ii) Fig. ??ab

Fluid (water)	Solid (steel)
$\rho_f = 1000\ kg \cdot m^3$	$\rho_s = 7900\ kg \cdot m^{-3}$
$\mathcal{K}_f = 2.1\ GPa$	$E = 210\ GPa$
	$\nu_s = 0.3$
	$R_0 = 0.395\ m$
	$e = 0.008\ m$
	$L = 20\ m$

[Physical properties and configuration for case (iii)]

Impacting rod system (iii) Fig. ??c

Fluid (water)	Solid (steel)	rod & sleeves (steel)
$\rho_f = 999\ kg \cdot m^3$	$\rho_s = 7985\ kg \cdot m^{-3}$	$M_0 = 1.312\ kg$
$\mathcal{K}_f = 2.14\ GPa$	$E = 168\ GPa$	$M_L = 0.3258\ kg$
	$\nu_s = 0.29$	$F_{rod} = 9.4\ kN$
	$R_0 = 0.02601\ m$	$V_{rod} = 0.1175\ m \cdot s^{-1}$
	$e = 0.003945\ m$	
	$L = 4.502\ m$	

TABLE 1. Physical parameters associated with the three configurations depicted in Figure **??**.

List of Figures

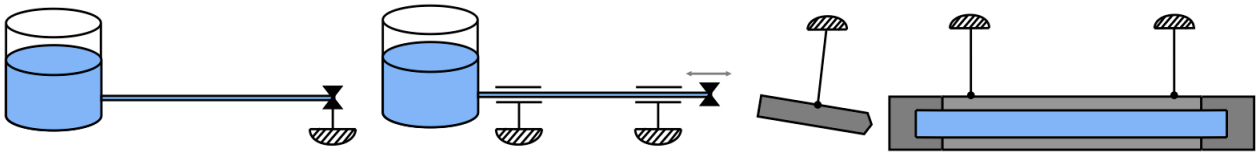

(a) Case (i): Anchored valve (b) Case (ii): Axially free valve (c) Case (iii): Impacting rod

Fig. 1. Boundary condition sets investigated for the liquid-filled pipe problem.

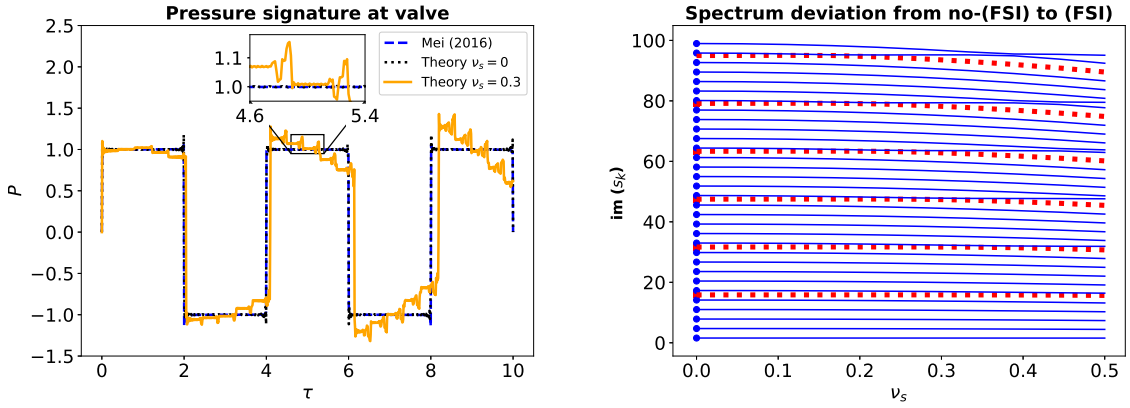

Fig. 2. Time-domain result and spectrum solution of test case (i). (a) Pressure response with FSI ($\nu_s = 0.3$ continuous brown lines) and without FSI modeling ($\nu_s = 0$ black dotted lines) versus Mei and Jing (2016)'s theoretical solution (which does not take into account FSI effects, i.e. for which $\nu_s \equiv 0$). (b) Spectrum (32 first eigenvalues) associated with Dirichlet/Dirichlet boundary conditions (19) versus the Poisson modulus ν_s (blue dots for $\nu_s = 0$ are Mei and Jing (2016)'s spectrum and red dots are the pure elastic modes the union of which compose the spectrum (25). As ν_s varies, some eigenvalues come close to one-another, but a careful inspection shows no cross-over between the depicted eigenvalues.

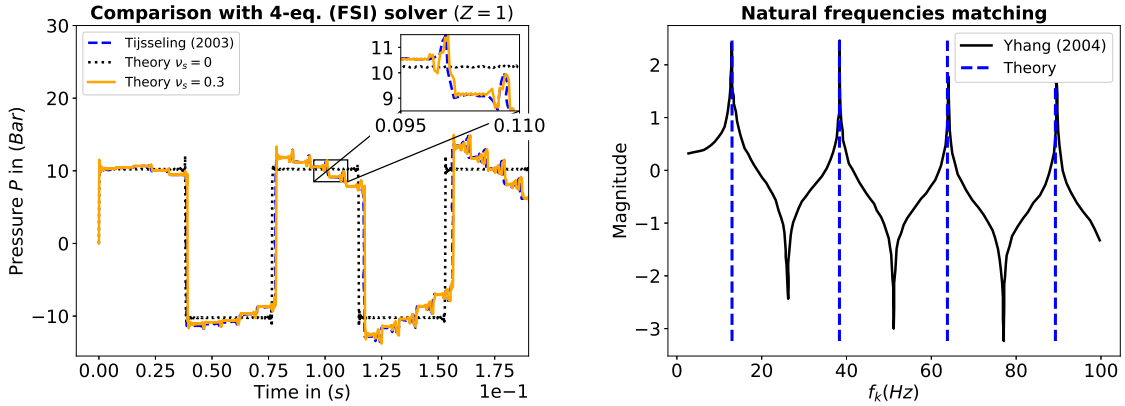

Fig. 3. Time-domain and frequency-domain results of test case (i). (a) Comparison between pressure field analytical solution at valve location (continuous brown lines) with MOC solutions provided by Tijsseling (2003) (dashed blue lines). Non-FSI solutions (i.e $\nu_s = 0$) are provided for illustration in black dotted lines. Insets provide a zoom for detailed check. (b) Comparison between Yang et al. (2004b)'s pressure prediction in frequency domain at valve position (continuous black line) and discrete spectrum eigenvalues obtained from transcendental equation (25) depicted in dotted (blue) lines.

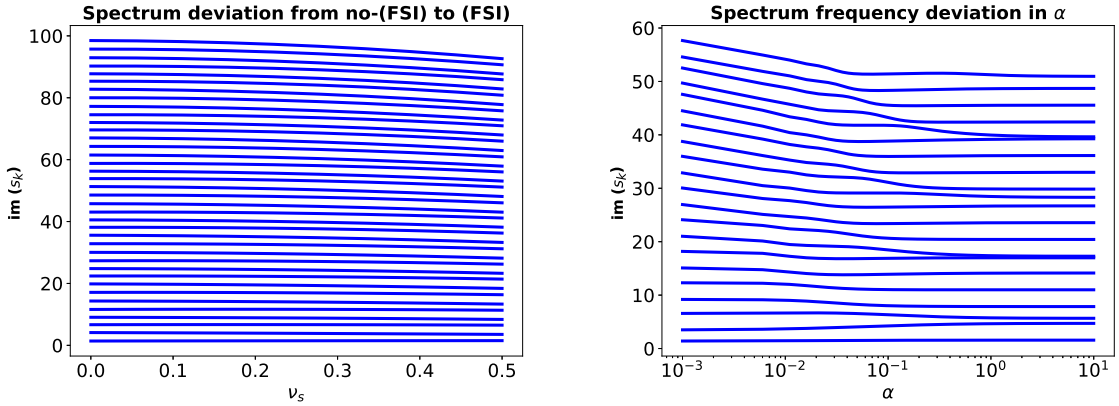

Fig. 4. Spectrum of case (ii). (a) first 38 eigenvalues evaluated from (38) versus the Poisson modulus ν_s. (b) first 21 eigenvalues versus the dimensionless pipe's thickness α. As α varies, some eigenvalues come close to one-another, but a careful inspection shows no cross-over between them.

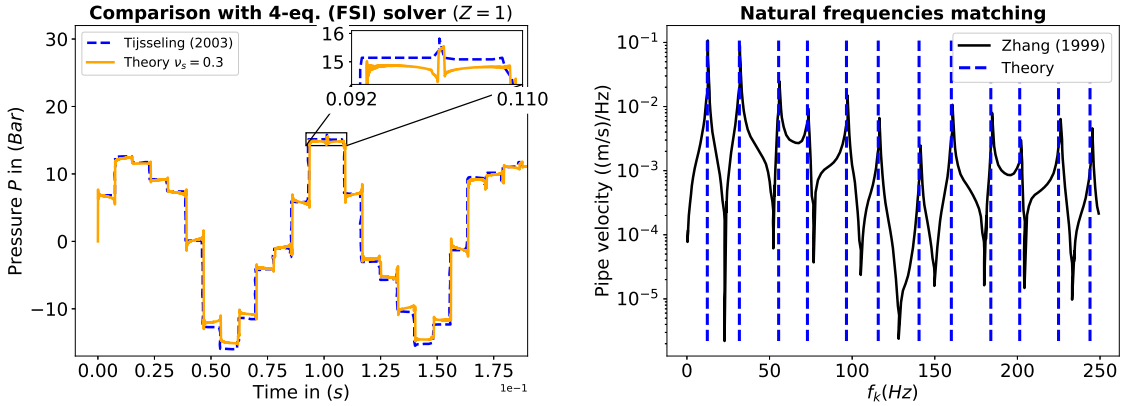

Fig. 5. Time-domain and frequency-domain results of test case (ii). (a) Comparison between pressure field analytical solution at valve location (continuous brown lines) with MOC solutions provided by Tijsseling (2003) (dashed blue lines). Insets provide a zoom for detailed check. (b) Comparison between Zhang et al. (1999)'s pipe velocity spectrum at valve and eigenvalues obtained from transcendental equation (38)

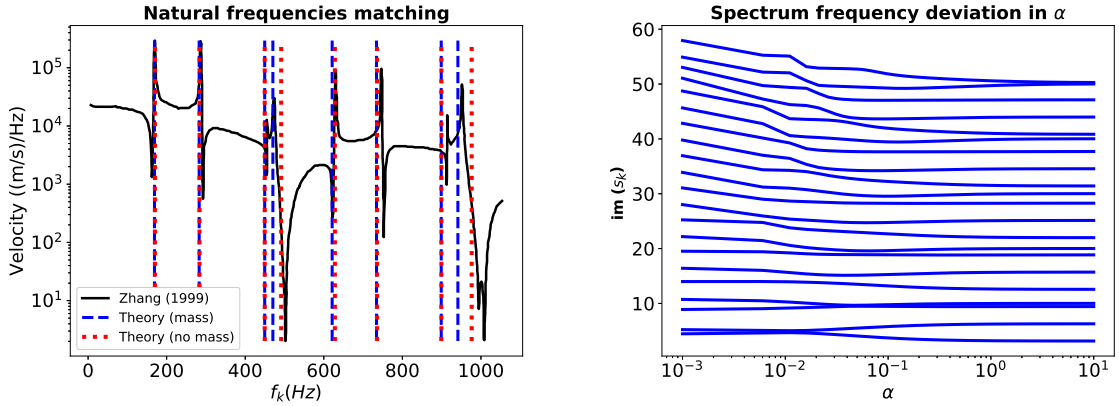

Fig. 6. Spectrum of case (iii). (a) Comparison between Zhang et al. (1999)'s pipe velocity spectrum at valve and eigenvalues obtained from the root of (55). Investigation of natural frequencies with (blue dashed line) or without (red dotted line) considering the sleeves masses is depicted. (b) first 21 eigenvalues versus the pipe's thickness / radius ratio α. As α varies, some eigenvalues come close to one-another, but a careful inspection shows no cross-over between the depicted eigenvalues.

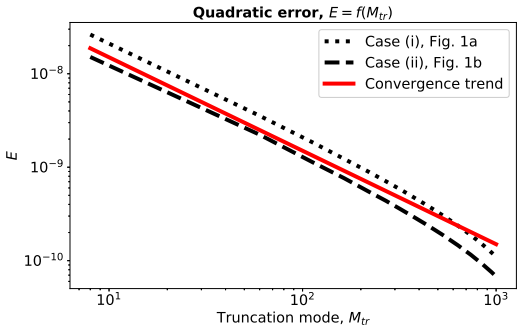

Fig. 7. Log-log plot of the truncation error E defined in (59) versus mode truncation M_{tr} for the analytical solutions of case (i) and (ii). A linear convergence M_{tr}^{-1} is depicted in (red) continuous line.